Nanoscale

Interface and Defect Engineering of Hybrid Nanostructures Toward an Efficient HER Catalyst

Journal:	*Nanoscale*
Manuscript ID	NR-COM-02-2019-001321.R1
Article Type:	Communication
Date Submitted by the Author:	08-May-2019

Complete List of Authors:	Özden, Şehmus; Los Alamos National Laboratory Bawari, Sumit; Tata Institute of Fundamental Research Centre for Interdisciplinary Sciences, Vinod, Soumya; Rice University Martinez, Ulises; Los Alamos National Laboratory Susarla, Sandhya; Rice University Narvaez Villarrubia, Claudia; Los Alamos National Laboratory, a. Physical Chemistry and Applied Spectroscopy (C-PCS), Chemistry Division; Los Alamos National Laboratory, mpa-11, Material Synthesis and Integrated Devices Joyner, Jarin; Rice University Tiwary, C.; Indian Institute of Science Campus Bangalore Narayanan, Tharangattu; Cochin University of Science and Technology Ajayan, Pulickel; Rice University

Interface and Defect Engineering of Hybrid Nanostructures Toward an Efficient HER Catalyst

Sehmus Ozden[1*], Sumit Bawari[2], Soumya Vinod[3], Ulises Martinez[1], Sandhya Susarla[3], Claudia Narvaez[1], Jarin Joyner[3], Chandra Sekhar Tiwari[4], Tharangattu N. Narayanan[2], Pulickel M. Ajayan[3]

[1]Materials Physics and Applications Division, Los Alamos National Laboratory, Los Alamos, NM, USA

[2]Tata Institute of Fundamental Research–Hyderabad, Sy. No. 36/P, Gopanapally Village, Serilingampally Mandal, Hyderabad–500 107, India

[3]Department of Material Science and NanoEngineering, Rice University, Houston, Texas, 77005 United States

[4]Metallurgical and materials Engineering, Indian Institute of Technology Kharagpur, Kharagpur-382355, INDIA

Abstract

The hydrogen evolution reaction (HER) plays a key role in hydrogen production for clean energy harvesting. Designing novel efficient and robust electrocatalysts with enough active sites and excellent conductivity is one of the key parameters for hydrogen production by water splitting devices. Recently, low-dimensional carbon materials have gained attention as metal-free catalysts for hydrogen production. Such nanostructures need to be engineered for improvement in their catalytic activity. Here, we designed and synthesized the B and N doped carbon nanostructures (CNS)-hBN heterostuructures for improved HER catalyst. The hBN layers on CNS could provide exposed defects and edges that act as active sites for proton adsorption and reduction. The composition, structure and chemical properties of the B and N doped CNS-hBN heterostructure were tuned to obtain excellent HER activity. Detailed morphological, structural and electrochemical characterization demonstrated that the synergistic effect rising from the interaction between B and N doped CNS and hBN structures contribute to enhance

electrocatalytic performances.To get more insight the role of defects and doping, we performed density functional theory (DFT) calculations on the CNS-hBN heterostructures.

Key Words: Interface Engineering, HER, Defect Engineering, 2D-heterostructures, Graphene-BN,

Introduction

Hydrogen is an excellent environment-friendly fuel and it can be produced by solar-driven water splitting devices[1-3]. One of the biggest challenges in developing new energy conversion technologies for water splitting devices is to develop suitable catalysts that can efficiently and stably catalyze the key electrochemical processes of water-splitting reactions[4-5]. However, if inexpensive and efficient electrochemical water-splitting devices can be fabricated, they provide very effective solutions to not just the energy problem, but also to the climate-change issues. Catalysts are one of the key components of water-splitting devices. Some issues related to existing catalysts are their comparatively high-cost and limited storage, which limit their large-scale applications in relevant clean energy technologies[5]. In this regard, the development of novel electrocatalysts that exhibit higher catalytic activity, longer durability, as well as lower cost could greatly facilitate the realization of clean energy[6-7]. Toward developing novel HER catalyst, various methods have been developed to tune the band gap and engineer the properties of materials including metal nanoparticles, 2D-nanosheets, nanotubes and their hybrid structures. Recently, the advent of low dimensional nanomaterials such as nanotubes, graphene and graphene-like 2D-nanomaterials have intrigued intensive studies because of their rich physical and chemical properties. Different type of low dimensional materials such as nanotubes, graphene, h-BN, MoS_2, WS_2 and their hybrid structures have received significant attention due to their excellent catalytic activity[8-13]. Extensive efforts have been undertaken to use these low-

dimensional materials as a cutting-edge HER electrocatalyst. Several key properties such as high conductivity, high activity, and stability, which can be improved by doping with heteroatoms, creating defects and active edges, is required for the development of an effective electrocatalyst[14, 15]. In addition, creating van der Waals interactions between these low-dimensional materials offers controlling the band gap and free energy of hydrogen adsorption (ΔG_H), which enhance the HER activity[12, 16] . Among all approaches, the heteroatom doping is considered is one of the most facile and effective strategies[17]. To date, various heteroatoms such as O, N, B, P, and S have been successfully doped into carbon-based nanostructures[18-20]. For example, it was shown that doping CNS with N and P atoms is very effective approach for enhancing the catalytic activity of graphene in hydrogen evolution reaction because of the new active sites[18]. Doping CNS with two or more of different elements is more efficient for improving the catalytic activities compared with doping with the single element since doping with multiple elements can create a unique electronic structure with a synergistic coupling effect between the used heteroatoms[21]. B and N are the most used heteroatoms for doping of CNS because of the differences in their electronegativity[22]. More importantly, recently it is shown that integration the hexagonal boron nitride domains (h-BN) into CNS can create unique heterostructures with control-over electronic properties[23, 24]. However, doping CNS with B and N heteroatoms and creating h-BN domains into or on the CNS for tuning their properties with a facile method still remain a challenge.

In this work, we used different ratios of ammonia borane (AB) and carbon nanostructures (CNS), which are graphene oxide (GO) and CNTs, and annealed under Ar/H_2 for 3 hours at 900 °C (Figure 1). As a result of annealing at high temperature, AB turns to hBN on the surface of CNS and dope CNS with B and N heteroatoms. This process creates robust physical interactions

between hBN and CNS and heteroatom doped defects and thus active sites. The layered restacking of hBN plates give rise to unique three-dimensional (3D) porous and large surface area CNS (Figure S1 and S5). Increasing the ratio of AB leads to rise in defect density and interface interactions between hBN and CNS. Thus, the number of active sites on the hBN-CNS increases and significantly enhances the hydrogen evolution reaction (HER) activity compared to pure porous networks of 3D-CNS foams. To gain further insights of the role of defects that contain heteroatoms on the adsorption of hydrogen on the surface of the structure, DFT calculations were performed.

Experimental

CNS-hBN hybrid porous architectures were fabricated by physically mixing AB and CNS with increasing amount of AB gradually as following; CNS:AB= 1:0.25, 1:0.5, 1:1, 1:2, 1:4 (Figure S1). The prepared mixture was annealed under Ar/H_2 at 900 °C for 3h, which resulted in heteroatom doped CNS and CNS-hBN hybrid structures (Figure 1). Density functional Theory (DFT) Method: DFT calculations are done using the SIESTA 4.0 package, considering a 96 atom (22 hBN and 74 C) system for hBN domain graphene (Figure 5A) and 58-59 atom(12-14 BN and 44-47 C) systems for defected hBN domain structures[25]. In a periodic unit cell of 12.7x12.3x15.8 $Å^3$, the CNS-hBN structure is periodic in nature. Pseudo potentials are generated using the generalized gradient approximation (GGA) Perdew–Burke–Ernzerhof (PBE) exchange correlation functional[26]. The spin un-polarised wave functions are used for energy and local density of states (LDOS) calculations. The energy cut-off for the real space grid is set at 500 Ry. The Broyden method in a variable-cell-relaxation scheme is employed for geometry relaxation. We use a 4x4x1 k-points sampling of the Brilliouin zone using the Monkhorst–Pack scheme[27]. The ΔG_H for hydrogenation in individual systemsis calculated using the following equation.

$\Delta G_H = E_{S-H} - E_S - 0.5E_{H2} - [T\Delta S + ZPE]$ where ZPE is the zero point energy correction, which along with $T\Delta S$ adds a constant value of 0.24 eV to obtain the corrected ΔG_H.

Results and Discussion

The density of rGO-1hBN and CNTs-2hBN are ~3.5mg/cm^3 and ~5mg/cm^3 respectively (Figure 1). The modifications of the surface of the CNS are confirmed using Raman spectroscopy[28]. Raman spectra of CNS typically has two characteristic peaks, G-band and D-band. G-band around 1530 cm^{-1} is closely related to vibrations of sp^2 hybridization of carbon, and D-band around 1350 cm^{-1} shows the sp^3 hybridized carbon structure, which mostly comes from defects on the honeycomb lattice of carbon (Figure 2a)[28, 29]. A quantitative defect density in the honeycomb lattice of CNS can be determined from the ratio between these two bands, I_D:I_G, which is quantifies to the structural changes as a result of heteroatoms doped defects and heterostructure of CNTs-hBN[30] . As seen in figure 2b I_D:I_G ratio increases with greater AB amount in the CNS since increased AB ratio give rise into the defect density by doping the hexagonal lattice of carbon with B and N. The intensity ratio between the D-band and G-band (I_D/I_G) increases from 0.25 to 1.41 for CNT-hBN and increased from 0.87 to 1.48 for rGO-hBN structures as the disorder of hexagonal carbon lattice as shown in the representative structure in figure 2c. FT-IR in figure 2d was used to determine the chemical bonds of heteroatoms and functional groups in the sample. The spectrum shows different functional groups of CNS at ~3350 cm^{-1} corresponds to O-H stretching vibrations, ~2950 cm^{-1} shows C-H stretching vibrations, ~1720 cm^{-1} corresponds to C=O stretching vibrations of carboxylic acids, ~1210 cm^{-1} presents C-OH stretching vibrations and ~1060 cm^{-1} shows the C-O stretching vibrations. In addition to these, the skeletal vibrations from unoxidized C=C bonds was seen at ~1620 cm^{-1}. The B-N-B in plane vibrations (E1u mode) for hBN was assigned to ~1380 cm^{-1} and the out of

the plane B-N-B vibrations (A2u mode) to ~810 cm^{-1} [31-33] . As a result of doping C-N stretching peak appeared around 1200 cm^{-1}. XPS analysis was used for quantitative chemical analysis of CNTs, GO, CNTs-2hBN and rGO-2hBN. The C1s core level peak positions of the carbon atoms are approximately at 285 eV and the peak position of oxygen is around 532 eV for both CNTs and GO (Figure S2). In high resolution XPS characterization of GO, the C-C, C-O, C=O and π-π bond peak is around 284.6 eV, 285.7 eV, 286.4 eV and 288.5 eV respectively (Figure S4)[34]. High resolution XPS of CNTs shows similar bonding with a small shifting (Figure S4). C-C, C-O, C=O and π-π bonding are correspond to 284.6 eV, 285.8 eV, 286.5 eV and 291.1 eV, respectively. The binding energies of N1s and B1s were found at 396.9 eV and 189.4 eV respectively in both CNTs and rGO samples after the growth of hBN (Figure S4). In high resolution XPS characterization of CNTs-2hBN and rGO-hBN, the C1s peak can be fitted in to peaks centered around 283.7, 284.4, 284.9, 286.2 and 286.8 eV due to sp^2 carbons of B−C, C−C, C-O/C=N, C−N/C=O and O-C=O bonds, respectively[35, 36] (Figure 2e-f).

To understand the morphology and structure of CNTs-2hBN and rGO-hBN hybrid nanostructures, a detailed microscopic characterization has been performed. Scanning Electron Microscopy (SEM) has revealed that the morphology of 3D structure of GO and CNTs consists of highly interconnected porous structures after freeze drying (Figure 3a, b). This 3D porosity makes these structures very promising catalysts for electrocatalytic applications since these porous electrodes can enhance the accessibility of active sites, improve the transport properties of reaction-relevant species and increase the electron transfer within whole electrodes. Figure 3c-d shows the transmission electron microscopy (TEM) images that clearly shows that rGO-hBN hybrid structures. The dark regions in figure 3c shows that hBN nanoflakes are decorated on the large area rGO nanosheets. Figure 3e shows the structure of as grown CNTs network that contain

iron particles. One of the key features of this structure is that it contain structural defects on the junction location, which improve the catalytic activity[37]. In addition to the existing defects in CNTs structures, it is clearly seen that merging of graphitic layers of hBN sheets onto CNTs give rise for better catalytic activity (Figure 3f-h). It indicates the interface between hBN and CNS reveals graphitic layers on both rGO and CNTs, which is considered to be the most significant region for hydrogen adsorption and desorption. BET surface analysis was performed to determine the surface area and porosity of CNTs, CNTs-2hBN, GO, and rGO-1hBN (Figure S5). The N_2 absorption indicates a type-II isotherm, which exhibits a negligible concave section, that is known to be keen to microporous volume uptake and a quick rise in total volume close P/P_0 = 1 signifying to macroporosity (Figure S5). The BET surface area (S_{BET}) area of CNT-2hBN and rGO-1hBN is 289 m^2/g and 313 m^2/g respectively, which is larger than the pristine CNTs (178 m^2/g) and GO (204 m^2/g). CNS and CNS-hBN samples shows similar average pore size distribution and the cumulative pore volume of CNS-hBN is higher than the pristine CNS samples.

Figure 4 shows the HER activity of pristine CNS and CNS-hBN hybrid structures. Figure 4a shows the linear sweep voltammogram (LSV) plots of the HER activity of the CNTs with gradually increased hBN ratio. The onset potential of the structures were determined by the intersection of two tangent lines. The HER activity increases with the increased hBN ratio. The onset potential value for pristine CNTs is -256 mV. The onset potential value increases to -243 mV, -234 mV, -206 mV and -196 mV for the CNTs:0.25hBN, CNTs:0.5hBN, CNTs:1hBN and CNTs:2hBN respectively. The catalytic activity of the structure starts to decrease with the ratio of CNTs-4hBN, which most probably because of the decreased conductivity with the increased insulator hBN ratio and defect saturations. The Nyquist plot of CNTs-2hBN showsthe smallest

semicircle in the low-frequency range, which indicate the lowest charge transfer resistance (Figure S6a). The EIS results confirm that the CNTs-2hBN displays a faster charge-transfer process during electrochemical reaction. The lowest onset potential (-164mV) with the highest current density (~42 mA cm^2) was achieved with the 1CNTs-2hBN sample. Here, the interconnection between individual CNTs, which includes defects and iron nanoparticles inside CNTs give rise to the HER activity[37]. We have observed similar trend for the rGO and hBN composition. As seen in figure 4b, the onset potential of pristine rGO is -264mV and the onset potential improves with increased amount of hBN. The lowest onset potential, 184 mV,was obtained with the 1rGO-1hBN ratio. In addition to the onset potential, the current density also enhances with the increased hBN ratio. The highest current density was achieved as ~31mA cm^2 with the 1rGO-1hBN sample. The reason for the improved onset potential and current density can be correlated with the defects created by doping with B, N heteroatoms and the interactions between CNS and hBN. The increased hBN ratio increases the heteroatom doping related defect density and B and N heteroatoms can replace the in-plane C-atoms or intercalate between the interlayer, which can donate electron or generate holes to effectively tune the electronic properties that can lead to lower conversion barriers for the transformation of H^+ ions to H_2. The dopant and interface interactions between hBN and CNS creates a synergistic effect, which can mediate the conductivity and catalytic activity of the final hybrid structures. More importantly, in-situ growth of hBN on CNS structures creates edges sites, which are more active than basal plane for CNS and hence the HER activity improves[12,38] . The onset potential of CNTs-2hBN and rGO-hBN drops to -262mV and -305mV respectively after 2000 cycles. Recently various reports showed the effect of heteroatom doping and heterostructures of 2D-nanosheets for improving the HER activity of catalysts. Figure S7 shows the comparison of the HER activity of

CNTs-2hBN and rGO-1hBN samples with some catalysis reported overpotential at 10 mA cm^{-2} in the literature. For example, S. Bawari and co-workers reported the improved HER activity of rGO by adding h-BN using solution processing[12]. They reported the overpotential of rGO-hBN 390mV at 10 mA cm^{-2}. In another example, Y. Zheng et. al. synthesized nitrogen (N) and phosphorus (P) dual-doped graphene as an efficient HER electrocatalyst[39]. They showed that the resultant N, P-graphene catalyst showed much lower HER overpotential is 420mV at at 10 mA cm^{-2} [39]. In addition, B. R. Sathe et al. reported B-doped graphene structure to improve the activity of metal-free electrocatalyst for HER showed overpotential 520mV at 10 mA cm^{-2} [38]. To evaluate the electrochemically active surface area (ECSA) electrochemically effective capacitance through a simple cyclic voltammetry (CV) were performed (Figure S6b, c). The specific capacitance was calculated from the CV curves according to the following equation

$$C = \frac{A}{\Delta V * \nu * m} \qquad (1)$$

Where A is the integral area of the cyclic voltammogram loop, ΔV is the sweep potential window, ν is the scan rate and m is the mass of the electrode materials at each electrode. The electrochemical capacitance associated with ECSA. The specific electrochemical capacitance of CNS samples increase with the increasing hBN ratio as shown in figure S6.

Figure 4c-d shows the Tafel plot of CNS-hBN structures, which is a convenient way for getting a better understanding of the kinetics and the mechanism of electrochemical reactions of CNS-hBN. The equation 1 for the overpotential includes two Tafel variables, the Tafel slope (β) and the exchange current density (j);

$\eta = \beta * \log j$ (1)

$H^+ + e^- \leftrightarrow H^*$ (2)

$H^* + H_3O+ + e^- \rightarrow H_2 + H_2O$ (3)

The Tafel slope is determined from the linear region within the Tafel plot. The lowest Tafel slope of CNTs based structure is CNTs-1hBN with 14.8 mV dec^{-1} value and the highest value belongs to 1CNTs-0.25hBN with 25.6 mV dec^{-1}. The rGO slope is the 25.8 mV dec^{-1} and the Tafel slope value of 1rGO-1hBN is 21.3mV dec^{-1}. Tafel plots of potential V–log j (current density) could be interpreted by the Volmer–Tafel or Volmer-Heyrovsky mechanism in the classical two-electron-reaction model for cathodic HER of CNS-hBN structures. The Tafel slopes of CNS in figure 4c-d suggests a typical Volmer–Heyrovsky mechanism. The Volmer step is initiating the HER by proton adsorption as shown in the equation 2. Doping CNS structures with B, N and synergistic interactions such as Van der Waals and π-π ineractions between CNS and hBN structures enhance the proton adsorption capacity[39]. In CNS-hBN structure, the edge of hBN is favorable for both adsorption of proton and desorption of molecular hydrogen gas. The Volmer step is followed by Heyrovsky step, where an adsorbed H atom and electron from the CNS-hBN structure react as shown in equation 3. Heyrovsky reaction is the second step that starts at a hydrogenated site on the CNS-hBN surface that formed by the previous Volmer reaction.

To study the apparent increase in HER activity for CNS-BN structures, we perform Density Functional Theory (DFT) calculations. TEM images show separate hBN and graphitic regions, as domains of hBN in the graphene lattice is structurally more stable when B, N source is provided simultaneously. The CNS-hBN structure is simulated by adding a smaller domain of hBN in a graphene lattice (Figure 5A). ΔG_H calculations on certain locations marked in A (Figure 5E), shows a decrease in ΔG_H (~0.9-1.1 eV) compared to pure hBN (3.34 (on Nitrogen) and 2.34 (on Boron) eV) and graphene (1.42 eV). These ΔG_H values show an approach towards

thermoneutral binding energy (~0 eV), but the drastic decrease in overpotential suggests that other active sites can also be present. In the synthesis process, AB and CNS are heated to very high temperatures where BN from AB bond to the graphitic lattice. In this process, a significant amount of defects are expected to form. To study the effect of defects, we study three types of defects, (5,8,5), (5,5,5,7,7,7) and point defects (or 5,9) which are shown in figure S8. The density of states (DOS) of all three types of defects (Figure 5B) shows that while the 5,8,5 and 5,5,5,7,7,7 type defects do not show many states near Fermi energy, in case of point defects of B and N the DOS at Fermi energy is very high. LDOS (Local Density of States) projections of these states shows a considerable occupation on nearby N and C in case of B point defect (Figure 5C), and on nearby B and N in case of N point defect (Figure 5D). Appreciably, the B point defect structure shows the highest DOS contribution and also the lowest ΔG_H of -0.0198 eV. While the N point defect structure has a ΔG_H of 0.428 eV, which is also considerably lower than the domain doped structure without defects.

Conclusion

In conclusion, we report the role of defects created by B, N doping and interface interactions of CNS-hBN by growing hBN on the CNS using AB that also acts as the source of doped heteroatoms, B and N. The hydrogen adsorption on the surface, conductivity, band gap and catalytic activity of CNS improve after growing hBN because of the defects created as a result of doping with B and N and the interface interactions between CNS-hBN is in favor of enhancing the catalytic activity. The HER activity of CNS structures improve with the increased amount of hBN, but after a certain amount of hBN the catalytic activity start to decrease, which is most probably because of the excess defects and insulating behavior of hBN. In addition, hBN edges

on the surface of CNS is improving proton adsorption and desorption of hydrogen gas. The Tafel slopes shows that the HER reaction follow Volmer−Heyrovsky and Volmer−Tafel mechanisms, which is two-electron-reaction that electron transfer steps convert adsorbed proton to hydrogen gas molecule. DFT calculations show that carbon atoms directly linked to hBN domains can act as efficient HER catalysts. Moreover, defects in the hBN domain introduces many more conducting states near Fermi energy, and such locations act as much better catalytic sites. Overall, this work signifies the role of the hBN-CNS interface with possible defects in generating highly active sites for HER.

Conflicts of interest

There are no conflicts to declare.

Acknowledgement

S.O. acknowledges financial support from a LANL Director's Postdoctoral Fellowship.

Corresponding Author

e-mail: sozden@lanl.gov

References

1. C. C. L. McCrory, S. Jung, I. M. Ferrer, S. M. Chatman, J. C. Peters, T. F. Jaramillo, J Am Chem Soc 2015, 137, (13), 4347-4357.
2. B. You, Y. J. Sun, Accounts Chem Res 2018, 51, (7), 1571-1580.
3. C. M. Wolff, P. D. Frischmann, M. Schulze, B. J. Bohn, R. Wein, P. Livadas, M. T. Carlson, F. Jackel, J. Feldmann, F. Wurthner, J. K. Stolarczyk, Nat Energy 2018, 3, (10), 862-869.
4. K. S. Joya, Y. F. Joya, K. Ocakoglu, R. van de Krol, Angew Chem Int Edit 2013, 52, (40), 10426-10437.
5. J. R. McKone, N. S. Lewis, H. B. Gray, Chem Mater 2014, 26, (1), 407-414.
6. P. C. K. Vesborg, B. Seger, I. Chorkendorff, J Phys Chem Lett 2015, 6, (6), 951-957.
7. N. Mahmood, Y. D. Yao, J. W. Zhang, L. Pan, X. W. Zhang, J. J. Zou, Adv Sci 2018, 5, (2).
8. D. H. Deng, K. S.Novoselov, Q. Fu, N. F. Zheng, Z. Q. Tian, X. H. Bao, Nat Nanotechnol 2016, 11, (3), 218-230.

9. Q. P. Lu, Y. F. Yu, Q. L. Ma, B. Chen, H. Zhang, Adv Mater 2016, 28, (10), 1917-1933.
10. X. Y. Yu, M. S. Prevot, N. Guijarro, K. Sivula, Nat Commun 2015, 6.
11. S. Li, S. S. Wang, M. M. Salamone, A. W. Robertson, S. Nayak, H. Kim, S. C. E. Tsang, M. Pasta, J. H. Warner, Acs Catal 2017, 7, (1), 877-886.
12. S. Bawari, N. M. Kaley, S. Pal, T. V. Vineesh, S. Ghosh, J. Mondal, T. N. Narayanan, Phys Chem Chem Phys 2018, 20, (22), 15007-15014.
13. C. B. Ma, X. Y. Qi, B. Chen, S. Y. Bao, Z. Y. Yin, X. J. Wu, Z. M. Luo, J. Wei, H. L. Zhang, H. Zhang, Nanoscale 2014, 6, (11), 5624-5629.
14. Y. F. Sun, S. Gao, F. C. Lei, Y. Xie, Chem Soc Rev 2015, 44, (3), 623-636.
15. J. T. Zhang, L. T. Qu, G. Q. Shi, J. Y. Liu, J. F. Chen, L. M. Dai, Angew Chem Int Edit 2016, 55, (6), 2230-2234.
16. S. Bawari, T. N. Narayanan, J. Mondal, J Phys Chem C 2018, 122, (18), 10034-10041.
17. J. Zhang, Z. Xia and L. Dai, Sci. Adv. 2015, 1, e150056.
18. J. Zhang, L. Qu, G. Shi, J. Liu, J. Chen, L. Dai, Angew. Chem. Int. Ed. 2016, 55, 2230 – 2234.
19. S. Guo, Z. Deng, M. Li, B. Jiang, C. Tian, Q. Pan, H. Fu, Angew. Chem. Int. Ed. 2016, 55, 1830 –1834.
20. Y. Ito, W. Cong, T. Fujita, Z. Tang, M. Chen, Angew. Chem. Int. Ed. 2015, 54, 2131 – 2136.
21. L. Ci, L. Song, C. Jin, D. Jariwala, D. Wu, Y. Li, A. Srivastava, Z. F. Wang, K. Storr, L. Balicas, F. Liu, P. M. Ajayan, Nat. Mater. 2010, 9, 430−435.
22. Y. Zheng, Y. Jiao, L. Ge, M. Jaroniec, S. Z. Qiao, Angew. Chem., Int. Ed. 2013, 52, 3110−3116.
23. H. Lim, S. I. Yoon, G. Kim, A. R. Jang, H. S. Shin, Chem. Mater. 2014, 26, 4891−4903.
24. J. Zhang, W. Xie, X. Xu, S. Zhang, J. Zhao, Chem. Mater. 2016, 28, 5022−5028.
25. J. M. Soler, E. Artacho, J. D. Gale, A. Garcia, J. Junquera, P. Ordejon, D. Sanchez-Portal, J Phys-Condens Mat 2002, 14, (11), 2745-2779.
26. J. P. Perdew, K. Burke, M. Ernzerhof, Phys Rev Lett 1996, 77, (18), 3865-3868.
27. J. D. Pack, H. J.Monkhorst, Phys Rev B 1977, 16, (4), 1748-1749.
28. M. S. Dresselhaus, A. Jorio, A. G. Souza, R. Saito, R. Philos T R Soc A 2010, 368, (1932), 5355-5377.
29. M. S. Dresselhaus, A. Jorio, M. Hofmann, G. Dresselhaus, R. Saito, Nano Lett 2010, 10, (3), 751-758.
30. S. Ozden, T. N. Narayanan, C. S. Tiwary, P. Dong, A. H. C. Hart, R. Vajtai, P. M. Ajayan, Small 2015, 11, (6), 688-693.
31. C. Gautam, C. S. Tiwary, S. Lose, G. Brunetto, S. Ozden, S. Vinod, P. Raghavan, S. Biradar, D. S. Galvao, P. M. Ajayan, P. M. Acs Nano 2015, 9, (12), 12088-12095.
32. S. Vinod, C. S. Tiwary, P. A. D. Autreto, J. Taha-Tijerina, S. Ozden, A. C. Chipara, R. Vajtai, D. S. Galvao, T. N. Narayanan, P. M. Ajayan, Nat Commun 2014, 5.
33. P. M. Sudeep, S. Vinod, S. Ozden, R. Sruthi, A. Kukovecz, Z.Konya, R. Vajtai, M. R. Anantharaman, P. M. Ajayan, T. N. Narayanan, Rsc Adv 2015, 5, (114), 93964-93968.
34. S. Ozden, C. S. Tiwary, J. Y. Yao, G. Brunetto, S. Bhowmick, S. Asif, R. Vajtai, P. M. Ajayan, Carbon 2016, 105, 144-150.
35. Y. H. Xue, D. S. Yu, L. M. Dai, R. G. Wang, D. Q. Li, A. Roy, F. Lu, H. Chen, Y. Liu, J. Qu, Phys Chem Chem Phys 2013, 15, (29), 12220-12226.

36. S. Ozden, T. Tsafack, P. S. Owuor, Y. L. Li, A. S. Jalilov, R. Vajtai, C. S. Tiwary, J. Lou, J. M. Tour, A. D. Mohite, P. M. Ajayan, Carbon 2017, 119, 142-149.
37. S. Ozden, C. S. Tiwary, A. H. C. Hart, A. C. Chipara, R. Romero-Aburto, M. T. F. Rodrigues, J. Taha-Tijerina, R. Vajtai, P. M. Ajayan, Adv Mater 2015, 27, (11), 1842-+.
38. B. R. Sathe, X. X. Zou, T. Asefa, Catal Sci Technol 2014, 4, (7), 2023-2030.
39. Y. Zheng, Y. Jiao, L. H. Li, T. Xing, Y. Chen, M. Jaroniec, S. Z. Qiao, Acs Nano 2014, 8, (5), 5290-5296.
40. S. Pal, M. Sahoo, V. T. Veettil, K. K. Tadi, A. Ghosh, P. Satyam, R. K. Biroju, P. M. Ajayan, S. K. Nayak, T.N. Narayanan, ACS Catal. 2017, 7, 2676−2684
41. J. Deng, P. Ren, D. Deng, X. Bao, Angew. Chem., Int. Ed. Engl. 2015, 54, 2100.
42. J. Yang, D. Voiry, S. J. Ahn, D. Kang, A. Y. Kim, M. Chhowalla, H. S. Shin, Angew. Chem., Int. Ed. Engl. 2013, 52, 13751.
43. D. Y. Wang, M. Gong, H. L. Chou, C. J. Pan, H. A. Chen, Y. Wu, M. C. Lin, M. Guan, J. Yang, C. W. Chen, Y. L. Wang, B. J. Hwang, C. C. Chen, H. Dai, J. Am. Chem. Soc. 2015, 137, 1587.

Interface and Defect Engineering of Hybrid Nanostructures Toward an Efficient HER Catalyst

Sehmus Ozden[1], Sumit Bawari[2], Soumya Vinod[3], Ulises Martinez[1], Sandhya Susarla[3], Claudia Narvaez[1], Jarin Joyner[3], Chandra Sekhar Tiwari[4], Tharangattu N. Narayanan[2], Pulickel M. Ajayan[3]

[1]Materials Physics and Applications Division, Los Alamos National Laboratory, Los Alamos, NM, USA

[2]Tata Institute of Fundamental Research–Hyderabad, Sy. No. 36/P, Gopanapally Village, Serilingampally Mandal, Hyderabad–500 107, India

[3]Department of Material Science and NanoEngineering, Rice University, Houston, Texas, 77005 United States

[4]Metallurgical and materials Engineering, Indian Institute of Technology Kharagpur, Kharagpur-382355, INDIA

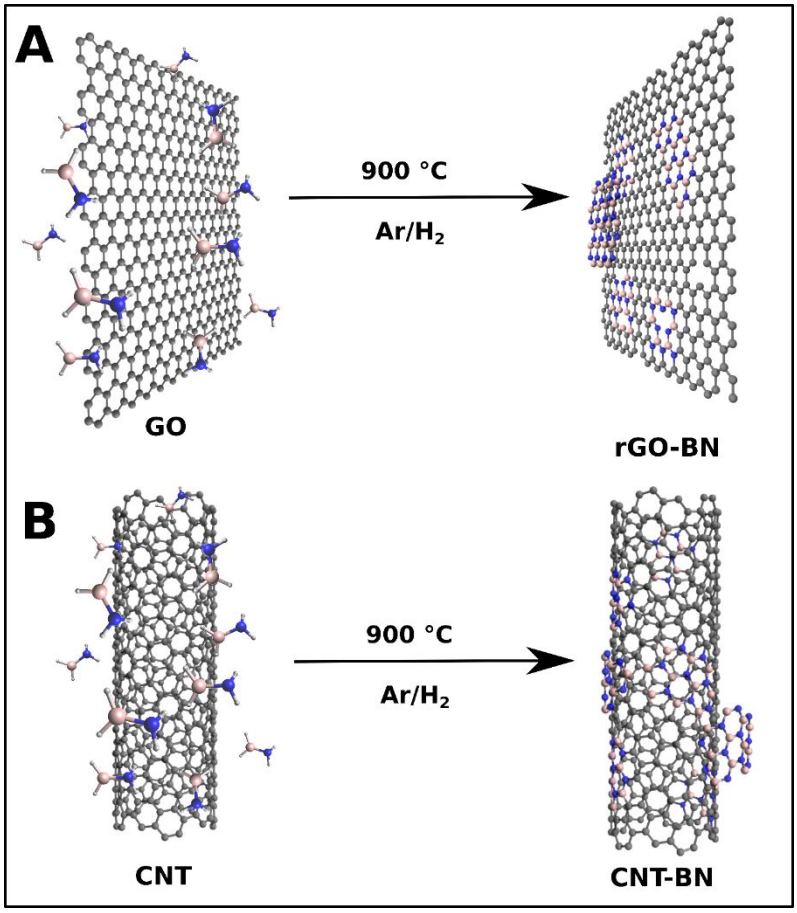

Figure 1. Schematic of CNS-BN synthesis (a) rGO-BN and (b) CNT-BN.

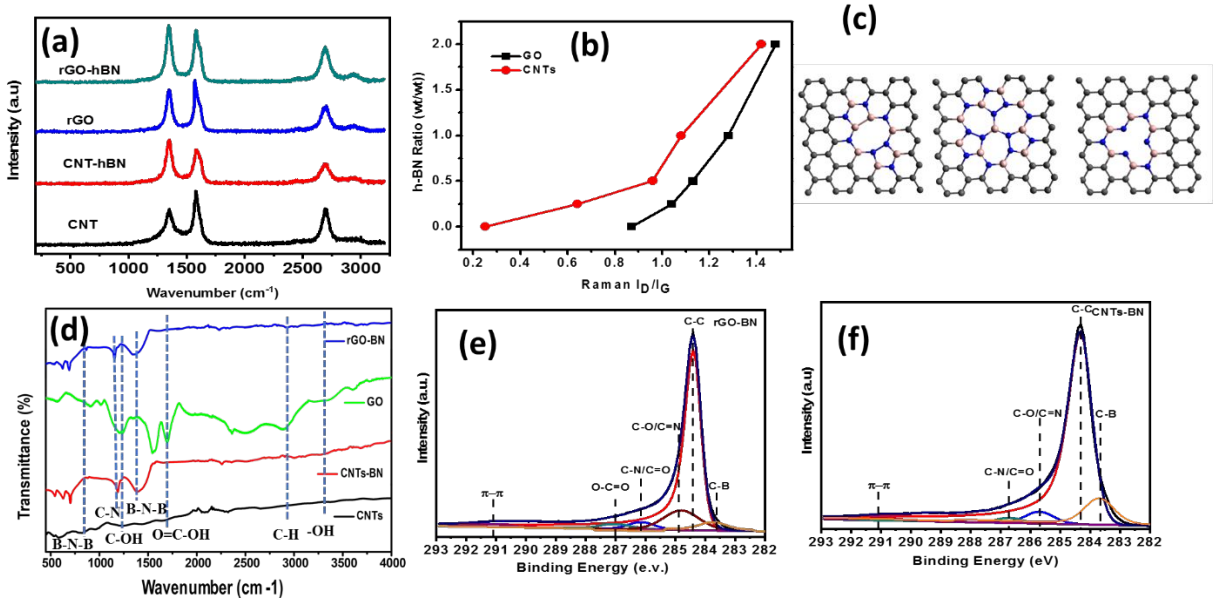

Figure 2. (a) Raman spectra of rGO, CNTs, 1rGO-1hBN and 1CNTs-1BN structures, (b) Defect density of CNS-BN heterostructures that obtained by I_D:I_G ratio of Raman spectra of CNS-BN

structures, (c) the schematic of defects created by doping with B, N and hybrid structure of CNS-hBN (d) FT-IR of CNS-BN heterostructures, (e) XPS spectra of 1rGO-1hBN and (f) XPS spectra of 1CNTs-1BN structures.

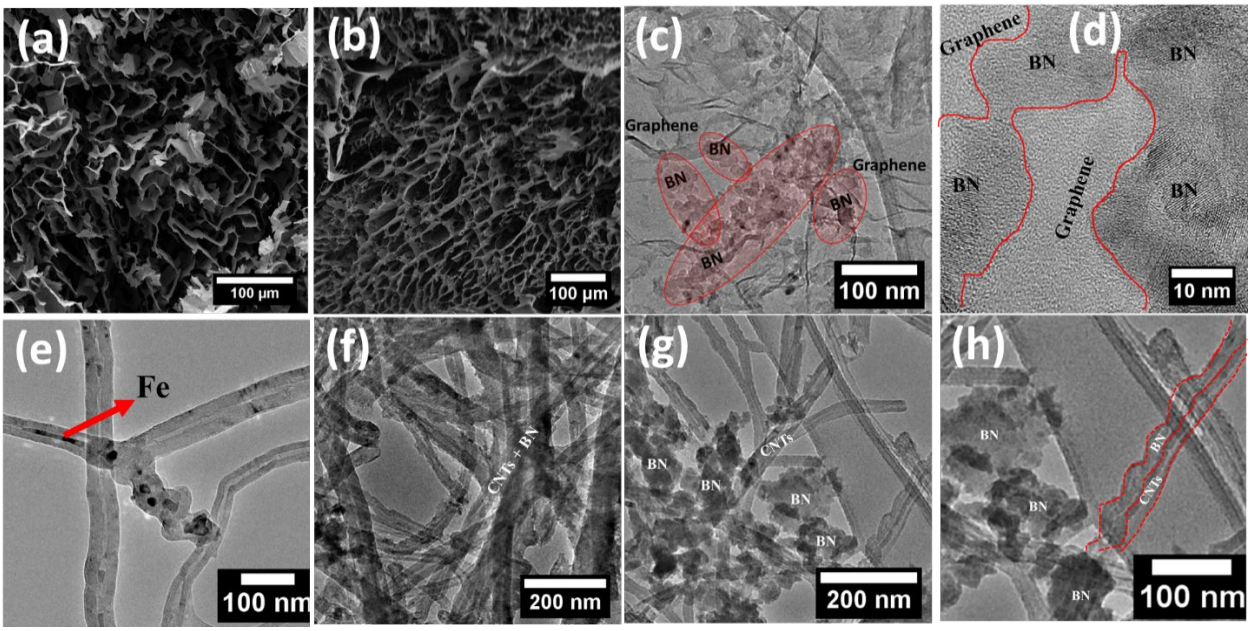

Figure 3. Microscopic characterization of CNS-BN structures. SEM images of porous structure of (a) GO and (b) CNTs. (c-d) HER TEM of rGO-BN heterostructures. (e) TEM images of interconnected CNTs filled with Fe. (f-h) TEM images of CNTs-BN hybrid structures.

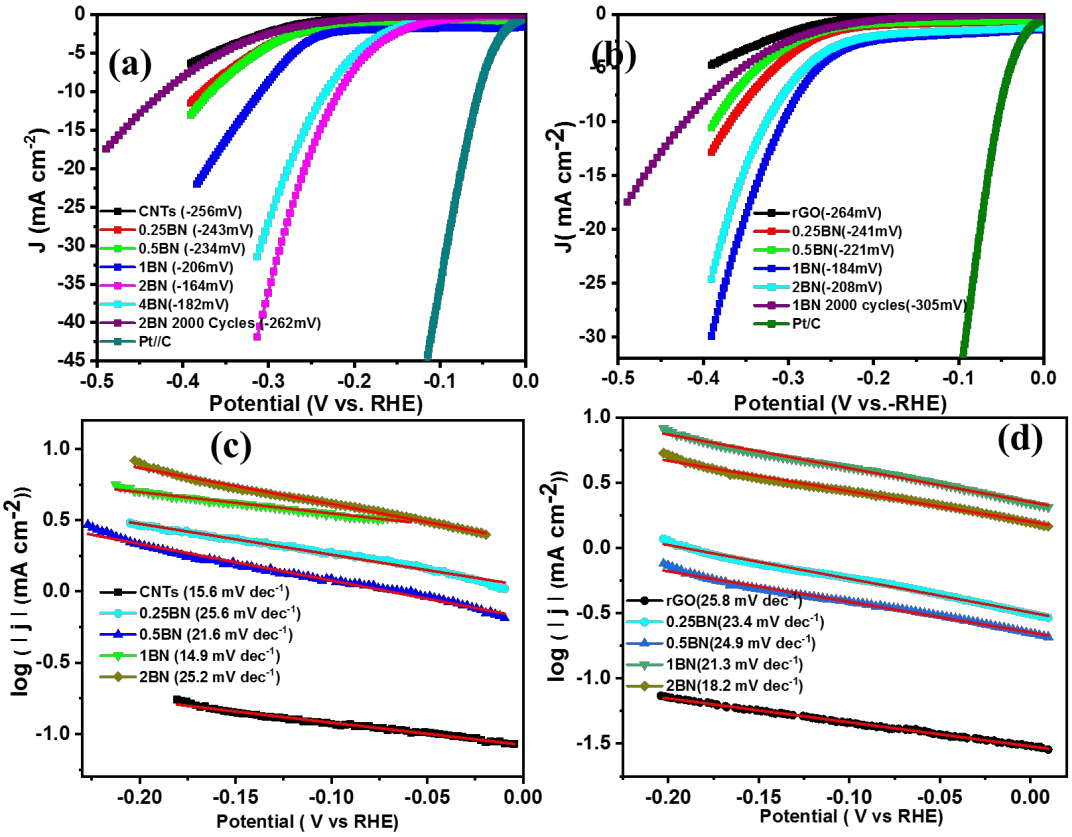

Figure 4. LSV plots of the HER activity of (a) CNTs-BN, (b) rGO-BN heterostructures, (c) Tafel plots of CNTs-BN and (d) Tafel plots of rGO-BN structures.

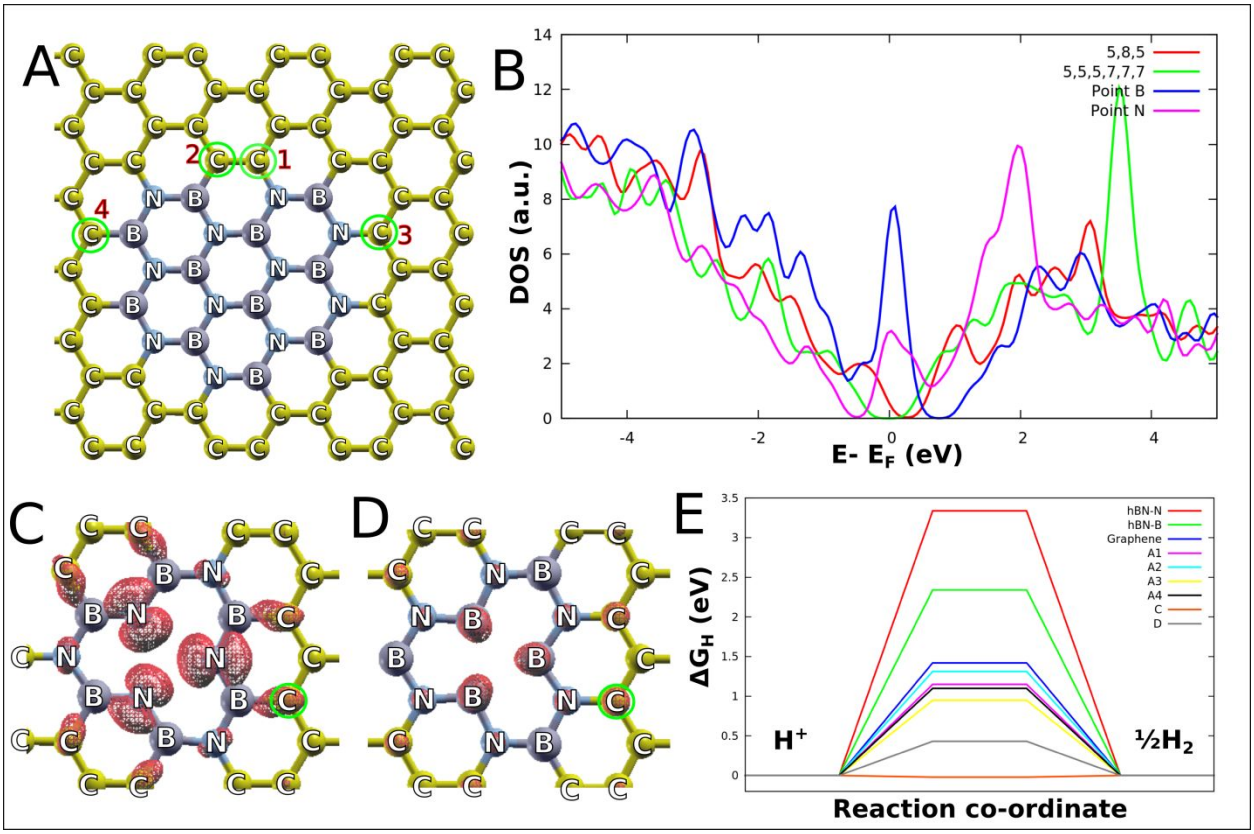

Figure 5. DFT calculations on CNS-BN. (A) Structure of domain doped BN in graphene. (B) Density of states (DOS) for defected BN domain doped graphene, with (5,8,5) , (5,5,5,7,7,7) and point defects of B and N shown in fig S5. (C-D) Local density of states (LDOS) near Fermi energy for B point defected and N point defected BN domain doped graphene. (E) Plot of delGH for pure hBN(B and N), graphene, and points shown in (A[1-4]), (C) and (D).